Acta Cryst. (1975). B31, 343

The Crystal Structure of $CaCO_3$(II), a High-Pressure Metastable Phase of Calcium Carbonate

BY LEO MERRILL* AND WILLIAM A. BASSETT

Department of Geological Sciences, The University of Rochester, Rochester, N.Y. 14627, *U.S.A.*

(*Received* 21 *March* 1974; *accepted* 13 *September* 1974)

Calcium carbonate, which crystallizes in the calcite structure at atmospheric pressure, transforms to $CaCO_3$(II) at 15 kbars and room temperature. This transformation is displacive and the $CaCO_3$ sample remains a single crystal in the $CaCO_3$(II) phase. Single-crystal X-ray data were obtained by using a newly designed miniature diamond-anvil gasketed pressure cell in which a small calcite rhomb was encapsulated in a purely hydrostatic medium. $CaCO_3$(II) is monoclinic, space group $P2_1/c$ with $a=6{\cdot}334\pm0{\cdot}020$, $b=4{\cdot}948\pm0{\cdot}015$, $c=8{\cdot}033\pm0{\cdot}025$ Å, and $\beta=107{\cdot}9°$. There are four molecules per unit cell, with all atoms in general positions 4(*e*). In the refinement of the positional and thermal parameters 112 independent reflections were used resulting in a residual $R_1=7{\cdot}8\%$. The transition involves both the rotation of carbonate groups by 11° and a small displacement of adjacent planes of calcium atoms parallel to one of the calcite $(10\bar{1}4)$ crystallographic planes. The transition mechanism is attributed to the condensation of a volume-dependent soft-phonon mode at the *D* point on the Brillouin zone boundary.

Introduction

Calcium carbonate crystallizes naturally with either the calcite [$CaCO_3$(I)] $R\bar{3}c$ or aragonite *Pmcn* structure. In calcite, which is the thermodynamically stable phase at atmospheric pressure and room temperature, each calcium atom is surrounded by six oxygen atoms, while in aragonite, the coordination is ninefold. For crystals of this class, the calcite or aragonite structure appears to be determined primarily on the basis of the size of the cation. Evans (1952) suggested that if the cation exceeds 1·1 Å, the aragonite structure is preferred. The radius of the calcium ion is very close to this value, which partially explains the commonly observed dimorphism in this material.

The calcium carbonate system has been studied extensively as a function of pressure and temperature but is still not completely understood. The main interest of most studies has been to determine the calcite–aragonite equilibrium phase boundary as accurately as possible. While calcite is stable at atmospheric pressure, aragonite is considered the stable high-pressure phase. A summary of the phase studies on the calcium carbonate system is presented in Fig. 1 with a comprehensive list of references to provide the reader with a background to this work.

Bridgman (1939) discovered two new room-temperature transitions at 14 and 17 kbar (now revised to 15 and 22 kbar) based on volumetric compression data. Both of the phases $CaCO_3$(II) and $CaCO_3$(III) occur within the commonly accepted stability field of aragonite, and since they have larger molar volumes, they are considered to be metastable with respect to aragonite. In order to understand the relationship of $CaCO_3$(II) and $CaCO_3$(III) to the stable phases and the various transformation mechanisms involved, it is very important to determine first their crystal structures.

Prior attempts to determine the $CaCO_3$(II) structure were based on X-ray powder diffraction studies by Jamieson (1957) and Davis (1964). Both these researchers noted the gradual disappearance of the calcite $11\bar{2}3$ reflection with increasing pressure. Jamieson (1957) suggested that this was due to anion disorder such as had been reported to occur in sodium nitrate at high temperatures. Davis (1964) presented evidence that the compression along the *c* axis was greater than that along the *a* axis, which is inconsistent with anion disorder, since it would require expansion along the *c* axis. Davis then proposed that $CaCO_3$(II) was isostructural with KNO_3(III), which has the $KBrO_3$-type structure space group $R3m$. Neither of these two explanations is consistent with our single-crystal data. A preliminary study employing single-crystal techniques (Weir, Block & Piermarini, 1965) also gave results that are not in agreement with the work described here.

It was not necessary to have pressure calibration capability in this experiment, as the presence of $CaCO_3$(II) single-crystal phase could be detected visually. At the calcite–$CaCO_3$(II) phase boundary, a Becke line moves across the crystal, indicating the transformation to $CaCO_3$(II). This feature was first pointed out by Van Valkenburg (1965), who showed that the single-crystal nature of the sample was preserved in the crystal structure transformation.

This paper deals principally with the analysis of experimental powder and single-crystal X-ray diffraction data of $CaCO_3$(II). Powder data were used for a determination of the lattice parameters, while single-crystal intensity data were used to solve the crystal structure. The displacive nature of the calcite–$CaCO_3$(II) transi-

* Present address: 574 HBLL, Brigham Young University, Provo, Utah 84602, U.S.A.

tion is discussed and compared with the pressure-induced ferroelectric transition in sodium nitrate. Finally, a plausible mechanism is proposed for the calcite–$CaCO_3$(II) transformation, based on the softening of a particular vibrational mode of the crystal.

Instrumentation and experimental procedure

$CaCO_3$(II) *single-crystal sample preparation*

For single-crystal X-ray diffraction studies, a new miniature diamond anvil pressure cell was developed (Merrill & Bassett, 1974), which was small enough to be attached to a standard goniometer head (Fig. 2). This pressure cell can be mounted interchangeably on the single-crystal orienter and the precession camera without any modification of the standard X-ray equipment.

The samples were encapsulated between the diamond faces within a 350 μm diameter hole in a piece of inconel foil 250 μm thick, known as the gasket. This process, first described by Van Valkenburg (1965), allows the solid sample to be subjected to a purely hydrostatic pressure. Glycerine was used as the pressure medium, since it does not vitrify within the range of this study.

Measurements were made on two separate crystals. A small cleavage rhomb was used as the sample from which the intensity data were collected on the diffractometer. The size of this crystal was dictated by two factors. It had to be large enough to produce detectable signals from the many low-intensity reflections and yet small enough to fit within the compressible gasket between the diamonds without being crushed by the anvils at the highest pressures. The cleavage rhomb was approximately $0{\cdot}3\times0{\cdot}2\times0{\cdot}06$ mm. Precession photographs were taken from a second sample crystal which was prepared by grinding and polishing a thin section of calcite perpendicular to the c axis.

Intensity measurements

The X-ray intensity measurements of $CaCO_3$(II) single-crystal reflections were made while the crystal was at an estimated pressure of 18 kbar. Angular scans of 3·3° were made of both the peak and background,

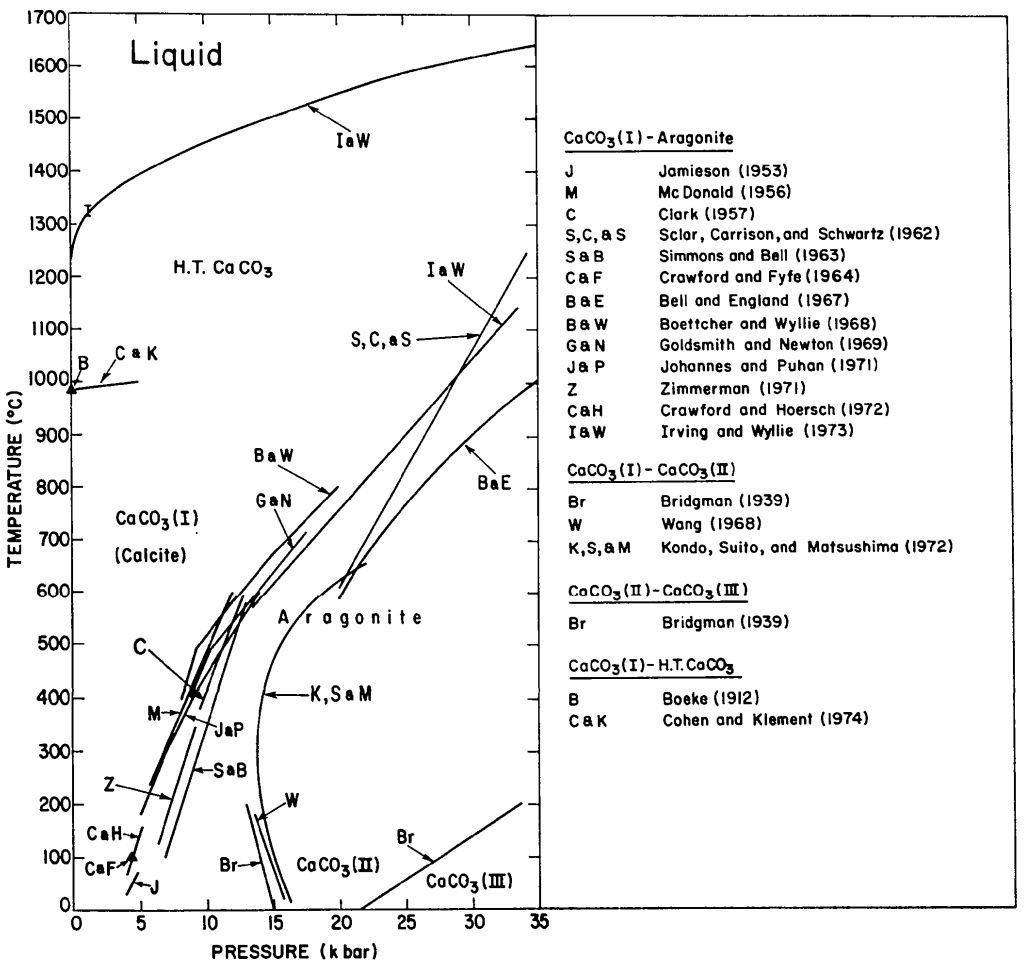

Fig. 1. Summary of reported data for phase boundaries of the $CaCO_3$ system: $CaCO_3$(I) (calcite, $R\bar{3}c$); aragonite, *Pbnm*; $CaCO_3$(II), $P2_1/c$; $CaCO_3$(III), *C*-centered; H. T. $CaCO_3$, structure not known.

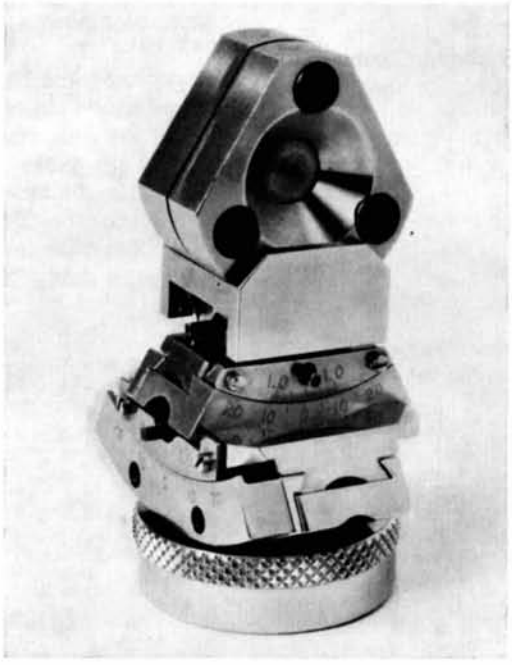

Fig. 2. Miniature diamond anvil pressure cell mounted on standard X-ray goniometer head.

To face p. 344

using the moving-counter moving-crystal method. Monochromatic Mo $K\alpha$ radiation was used, and scattered X-ray reflections were detected with a scintillation counter. A quartz presample monochromator was used to prevent white radiation streaks from the relatively large diamond anvils. The calcite rhomb was oriented in the pressure cell so that its $10\bar{1}4$ and $\bar{1}104$ reciprocal-lattice vectors were both in the $\chi=0$ plane.

In total, 164 reflections were measured, for which the intensity was greater than the background. All intensities were corrected for Lorentz and polarization factors. No additional polarization correction was made for the monochromator, since in the range of this study the correction for a quartz monochromator using Mo $K\alpha$ radiation is negligible.

The intensities were also corrected for absorption of the incident and diffracted X-ray beams by the beryllium and the diamond anvils. This correction was made as a function of the angles δ_1 and δ_2 which the axis of the pressure cell makes with $\mathbf{S}_0$, the incident, and $\mathbf{S}$, the diffracted X-ray beams respectively. The intensities of equivalent reflections were then averaged, resulting in 112 independent reflection intensities, which were then converted to F values (Table 1).

Table 1. *Comparison of observed and calculated F values from single-crystal data for* $CaCO_3$(II)

H	K	L	FOBS	FCAL	H	K	L	FOBS	FCAL	H	K	L	FOBS	FCAL
0	0	-2	20.5	-15.7	3	-2	1	20.0	-24.7	-2	-3	4	29.8	27.3
1	0	-2	17.2	15.6	0	-2	2	61.5	53.7	2	-3	4	35.7	24.1
2	0	-4	59.9	-61.7	1	-2	2	42.8	43.2	-3	-3	4	34.8	29.7
0	0	-4	26.6	23.3	1	2	-2	29.6	-30.9	0	-3	-6	25.7	-29.5
1	0	-6	19.7	21.6	2	-2	2	35.2	-35.3	1	3	-6	22.0	22.2
2	0	-6	23.8	23.7	-2	-2	2	51.0	-53.6	-1	3	-6	6.5	-7.3
3	0	-6	20.1	-19.9	1	-2	3	22.5	20.5	3	3	-6	25.9	-26.1
3	0	-8	35.4	36.8	0	-2	4	25.5	-28.3	-2	-3	6	24.7	-23.2
1	0	-8	30.4	-31.5	1	2	-4	12.7	13.4	-6	-3	6	20.1	16.5
0	0	-8	13.5	11.4	1	-2	4	24.8	-26.6	2	3	-8	18.6	22.9
1	-1	0	8.4	-15.2	-2	2	-4	23.5	23.0	2	-4	0	43.3	-44.3
0	1	-2	17.2	-16.4	2	2	-4	27.3	29.1	2	4	-1	20.0	-17.1
0	-1	2	17.2	-16.4	-3	-2	4	11.1	-10.1	0	-4	2	14.5	-15.0
1	-1	2	39.3	41.4	1	-2	-5	21.8	23.2	1	-4	2	11.6	-11.9
0	-1	-3	38.5	39.5	1	-2	-6	33.4	-33.5	-1	-4	2	6.9	6.3
-1	1	-3	5.8	5.0	2	2	-6	14.3	-15.5	2	-4	-2	28.3	26.4
0	-1	-4	28.8	-29.9	3	2	-6	36.1	34.3	6	-4	2	11.6	10.8
1	1	-4	41.9	41.9	-1	2	-7	13.3	-12.5	0	-4	4	38.1	37.7
-1	1	-4	26.5	-26.8	1	2	-8	22.6	22.6	-1	-4	4	28.0	-23.2
2	1	-4	33.6	-31.3	2	2	-8	9.0	7.9	-2	-4	4	36.9	-36.1
0	-1	-5	12.6	13.8	3	2	-8	24.4	-24.2	2	-4	4	22.3	-19.7
1	1	-5	7.2	-7.8	4	2	-8	9.5	-9.8	1	4	-8	22.6	-26.7
2	1	-5	19.7	-20.0	1	2	-6	32.0	-33.5	-1	4	-8	21.4	24.8
0	1	-6	41.9	-35.4	2	2	-10	10.6	11.0	3	4	-8	23.1	23.6
1	-1	-6	14.9	15.8	-1	-3	0	43.9	-46.8	4	4	-8	15.7	16.9
-1	1	-6	20.7	21.5	-3	-3	3	9.3	6.9	1	-5	0	20.1	-22.2
2	-1	-6	37.3	-35.4	0	-3	-1	18.9	24.1	0	-5	2	19.6	-18.6
3	1	-6	18.8	18.0	1	-3	1	17.5	-15.3	1	-5	2	30.8	32.2
1	1	-7	10.1	-8.9	0	-3	-2	6.6	-6.1	-1	-5	2	29.5	-29.6
2	1	-7	12.9	-11.9	2	-3	2	17.3	-16.3	0	-5	4	17.0	18.5
0	1	-8	34.1	31.5	-2	-3	2	7.7	-8.4	-1	-5	4	9.8	8.8
1	-1	-8	11.7	11.2	1	-3	-2	34.8	-35.0	-9	-5	4	10.2	11.3
-1	1	-8	12.7	12.1	1	-3	2	53.5	-47.9	0	-5	10	13.1	-16.3
2	1	-6	25.8	-27.0	0	-3	2	6.1	6.1	0	-6	0	22.9	-21.4
3	1	-8	9.0	-6.1	0	-3	4	27.8	-29.2	-3	-6	6	20.5	16.1
2	1	-10	18.1	19.7	1	-3	4	6.2	7.3	-6	-6	6	15.9	10.5
0	-2	0	46.9	-45.9	-1	-3	4	14.3	-13.7	0	-8	0	23.4	19.6
1	-2	-1	33.9	-32.6										

Powder data

X-ray diffraction patterns were taken of a $CaCO_3$(II) powder sample encapsulated hydrostatically in the same manner as the single-crystal sample. The purpose of this study was to furnish lattice parameters and show that both the powder and single-crystal results of this study are in agreement, since previously reported powder intensities did not agree with our single-crystal data.

The lattice parameters of $CaCO_3$(II) were calculated from a least-squares refinement (Mueller, Heaton & Miller, 1960) of the d values taken from X-ray films. The crystallographic data of $CaCO_3$(II) and calcite are compared in Table 2, and the powder data of $CaCO_3$(II) are summarized in Table 3.

Table 2. *Crystallographic data for calcite and* $CaCO_3$(II)

	Calcite, 1 bar		$CaCO_3$(II), 15 kbar
Crystal system	Rhombohedral	(Hexagonal)	Monoclinic
Space group	$R\bar{3}c$		$P2_1/c$
a	6·391 Å	(4·989 Å)	6·334 Å
b			4·984
c		(17·062)	8·033
α/β	46·1°		107·9°
ϱ	2·71 g cm^{-3}		2·77 g cm^{-3}
Z	2		4
Volume of unit cell	122·6 Å^3		241·3 Å^3

Table 3. *X-ray diffraction powder pattern of* $CaCO_3$(II) *at approximately 15 kbar*

h	k	l	d(obs)	d(calc)	I/I_o*
0	1	1	4·110†	4·150	5
0	0	2	3·816	3·827	15
1	1	0		3·826	
1	0	−2		3·793	
2	0	0	2·998	3·016	100
1	1	−2		3·013	
2	0	−2	2·798	2·820	5
0	2	0	2·470	2·474	15
1	1	2		2·483	
0	1	3	2·264	2·268	20
1	2	−1		2·268	
2	1	1		2·267	
1	2	1	2·113	2·125	2
2	1	−3		2·110	
2	0	2	2·064	2·077	20
0	2	2		2·077	
1	2	−2		2·072	
1	1	3	1·954	1·960	5
2	2	−1		1·947	
2	0	−4	1·886	1·891	20
3	1	−2		1·898	
1	1	−4	1·869	1·862	20
3	1	0		1·866	
2	2	−2		1·863	
2	2	1	1·773†	1·775	2
2	1	−4		1·775	
1	0	4	1·690†	1·687	2
1	2	3	1·604	1·611	10
0	3	1		1·612	
1	1	4		1·591	
2	2	2		1·596	
1	3	0		1·591	
0	2	4	1·518	1·515	10
1	3	−2		1·513	
3	1	2		1·520	
4	0	0		1·518	

* Visual estimate of I/I_o.
† New reflections appearing in powder pattern.

Symmetry and structure of $CaCO_3$(II)

As soon as the $CaCO_3$(II) single-crystal X-ray data were obtained, it became evident that some simple relationship existed between $CaCO_3$(II) and the calcite structure. The most significant feature noted was that approximately two thirds (106 out of 164) of the reciprocal-lattice points with non-zero intensity corresponded to a slightly distorted calcite reciprocal lattice, with the remaining third being new reflections. These 58 additional reciprocal-lattice points are systematically located at points midway between allowed calcite reciprocal-lattice points in rows parallel to $10\bar{1}4$ [*i.e.* parallel to **a*** in Fig. 3(*d*)].

The change in metric symmetry between calcite and $CaCO_3$(II) is illustrated in Fig. 3, which shows the effect of the superposition of this new set of reciprocal-lattice points (represented by closed circles) with those of a slightly distorted calcite structure (represented by open circles). Figs. 3(*a*) and 3(*c*) show the *hk*0 and *h*0*l* zones of the calcite reciprocal lattice, while Figs. 3(*b*) and 3(*d*) show the corresponding zones for $CaCO_3$(II). The data of Fig. 3(*b*) are taken from a precession photograph, which combined with upper-level data from Fig. 3(*d*) reveal a complete loss of rotational symmetry about the former calcite **c*** axis. Further examination of the $CaCO_3$(II) reciprocal lattice also reveals that the highest symmetry remaining is a twofold rotation about the axis labeled **b***. The reciprocal-lattice vectors **a*** and **c***, which are perpendicular to **b***, were selected so that the volume of the unit cell was a minimum and the β angle was as close to 90° as possible.

With this assignment of basis, the conditions on *hkl* for observed reflections are summarized as follows: *hkl*, no conditions (*P*); *h*0*l*, $l=2n$ (*c*); 0*k*0, $k=2n$ (2_1).

On the basis of the observed extinctions and the metric of the reciprocal lattice, the space group of $CaCO_3$(II) is $P2_1/c$ (monoclinic). A comparison of the symmetry elements for $CaCO_3$(II) is made with those of calcite in Table 4.

Table 4. *A comparison of the symmetry elements of calcite and monoclinic* $CaCO_3$(II)

Symmetry element	Calcite ($R\bar{3}c$)	$CaCO_3$(II) ($P2_1/c$)
Trigonal axis	1	0
3_1 screw axis	1	0
Twofold axis	3 equivalent	0
2_1 screw axis	3 equivalent	1
Axial *c*-glide	3 equivalent	1*
Diamond glide	3 equivalent	0
Inversion symmetry	Yes	Yes

* Owing to the new indexing one of the diamond glides in the calcite structure becomes the *c*-glide in $CaCO_3$(II).

A comparison of the relative F_o of equivalent reflections was made in order to be certain that the true symmetry was indeed monoclinic, as indicated from the metric of the reciprocal lattice. The intensity data for the structure refinement of $CaCO_3$(II) were collected from a transformed calcite rhomb. In order to make a better comparison of equivalent reflections, a new crystal with the calcite *c* axis parallel to the axis of the pressure cell was studied by the precession method. In this orientation equivalent reflections in either the calcite or $CaCO_3$(II) phase encounter equivalent absorption paths through the pressure cell. An analysis of two levels of the monoclinic reciprocal lattice indicates the existence of a mirror plane perpendicular to **b***. Further analysis confirmed that the *F* values of 46 pairs of equivalent reflections from diffractometer data were

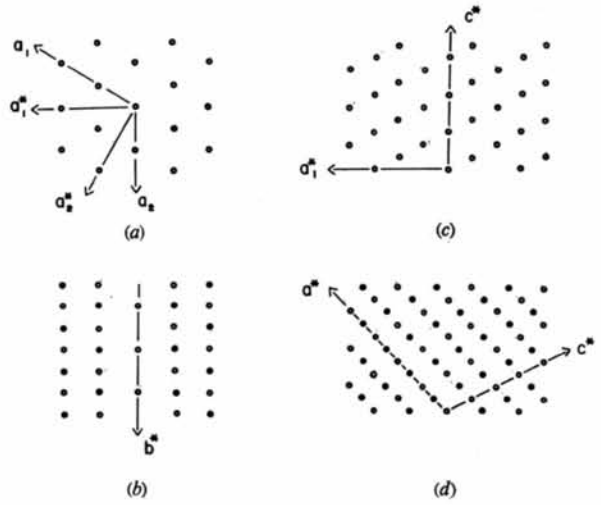

Fig. 3. (*a*) *hk*0 zone reflections of calcite taken from precession camera data. (*b*) Precession camera data for $CaCO_3$(II) taken from same orientation as (*a*) above. The reflections which were present in calcite are shown as open circles and new reflections are shown as solid circles. (*c*) An *h*0*l* zone of the calcite reciprocal lattice ($R\bar{3}c$). (*d*) The same projection as (*c*) above for $CaCO_3$(II). Reflections new to the $CaCO_3$(II) phase are shown as solid circles.

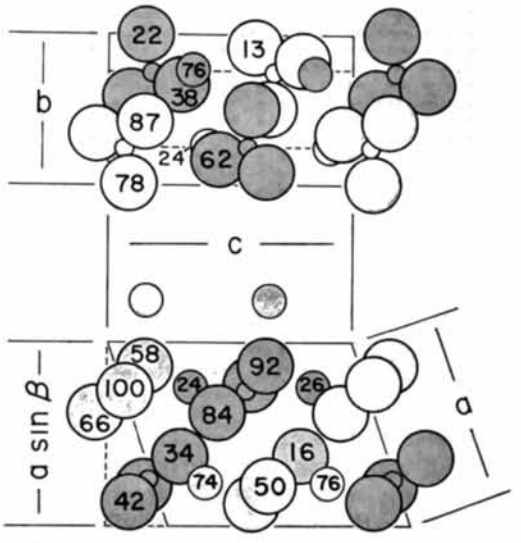

Fig. 4. The monoclinic $CaCO_3$(II) structure projected along *a* sin β (top) and along the *b* axis (bottom).

within $\pm 3\sigma$ of their respective mean, after being corrected for absorption.

The solution of the $CaCO_3$(II) structure was based upon the assumptions that calcium carbonate could be treated as a heavy-atom problem and the atomic positions could be obtained directly from the Patterson map. Using this method, the positions of calcium, carbon, and two oxygens were located, leaving the position of the third oxygen unresolved. The coordinates of the known atoms were used to calculate a Fourier map in which the final oxygen atom was located.

In the structure refinement (Busing, Martin & Levy, 1971) temperature factors were isotropic throughout and were initialized to the corresponding values for calcite. Atomic scattering factors for Ca^{2+}, O^{2-}, and C^0 were used (Cromer & Mann, 1968). Empirical standard deviations for the observations F_o were calculated from a least-squares fit of the curve

$$\Delta F = \sum_n a_n |F_o|^n$$

where ΔF is an estimate of $\sigma_{|Fo|}$. ΔF is the residual $|F_o| - |F_c|$ of a structure refinement with unit weights. Standard deviations for the observations are given by the linear equation

$$\sigma_{|F_o|} = 2{\cdot}475 + 0{\cdot}025|F| \ .$$

In the final structure refinement, using the above weighting scheme, all parameters were allowed to vary until the change on a given cycle was about $\frac{1}{10}$ of a standard deviation. The final cycle gave the residuals $R_1 = 0{\cdot}078$ and $R_2 = 0{\cdot}104$ where

$$R_1 = \||F_o| - |F_c|\|/|F_o| \ ,$$
$$R_2 = [\textstyle\sum w|\Delta F|^2 / w|F_o|^2]^{1/2} \ .$$

The standard deviation $\sigma_1 (= [\sum w|\Delta F|^2/(n-m)]^{1/2})$, for an observation of weight w, is 1·5. The positional and thermal parameters are listed in Table 5.

Table 5. *Atomic positional and thermal parameters for monoclinic* $CaCO_3$(II)

All atoms are in 4(*e*) general positions, space group $P2_1/c$.

	x	*y*	*z*	*B*(Å²)
Ca	0·234 (2)	0·738 (2)	0·217 (1)	0·48 (10)
C	0·260 (8)	0·253 (9)	0·504 (3)	0·93 (32)
O(1)	0·380 (7)	0·156 (3)	0·637 (3)	1·50 (38)
O(2)	0·134 (7)	0·088 (4)	0·381 (3)	2·13 (39)
O(3)	0·221 (6)	0·490 (4)	0·467 (3)	1·31 (34)

Description of the structure

The structure of $CaCO_3$(II) based upon the parameters of Table 3 is illustrated in Fig. 4. In an examination of this structure, some significant features are noted. The orientations of the monoclinic *a* and *c* axes are parallel to the former calcite $(01\bar{1}2)$ and $(10\bar{1}4)$ crystallographic planes respectively. The changes in atomic positions can be accounted for by the rotation of carbonate groups by 11° and the displacement of alternate planes of calcium atoms along the monoclinic *c* axis in nearly antiparallel directions.

Comparison of $CaCO_3$ *with* $NaNO_3$

In this section, we will contrast the calcite–$CaCO_3$(II) transformation with a pressure-induced transformation in $NaNO_3$, reported by Barnett, Pack & Hall (1969). This is of interest since both $CaCO_3$ and $NaNO_3$ have the calcite ($R\bar{3}c$) structure in nature, and although their displacive transitions each involve rotations of anions and displacements of cations, the mechanism in each case is significantly different. The transition in $NaNO_3$ apparently involves a continuous change from the paraelectric to the ferroelectric state, in which nitrate groups undergo a rotation and sodium atoms are displaced slightly from their position of $\bar{3}$ symmetry in a direction parallel to the trigonal axis. The rotation of the nitrate groups initiates at 49 kbar, and is strongly pressure dependent, attaining a maximum angle of 13° at 70 kbar. This transformation removes the inversion symmetry in $NaNO_3$, changing from space group $R\bar{3}c$ to $R3c$. The coupled motion of the rotation of nitrate groups and the simultaneous displacement of an adjacent layer of sodium atoms parallel to the *c* axis requires that all the nitrate groups within a given layer rotate in the same direction [Fig. 5(*a*)]. The displacements of sodium atoms within a given crystal domain are all in the same direction along the polar axis.

In order to compare the details of the pressure-induced $NaNO_3$ and $CaCO_3$ transitions, the cation sites of Fig. 5 have been labeled (*a*), (*b*), (*c*), and (*d*). In $NaNO_3$ the displacement (lowering) of a sodium atom in either an (*a*) or (*c*) site towards the nitrate layer is coordinated with a clockwise rotation of the nitrate groups below and a counterclockwise rotation of the nitrate groups above. The displacement of a sodium atom in either (*b*) or (*d*) sites away from the nitrate layer is similarly coordinated with a counter-clockwise rotation of the nitrate groups below, and a clockwise rotation of those above. Consequently, in the ferroelectric $NaNO_3$ transition, nitrate groups in adjacent layers will rotate in opposite directions, while the entire cation sublattice is displaced slightly along the polar axis with respect to the anion sublattice. The result of this type of motion is the loss of the center of symmetry.

In the $CaCO_3$(I)–$CaCO_3$(II) transition, however, the carbonate groups in a given layer do not all rotate in the same direction as in the ferroelectric sodium nitrate transition. Since $NaNO_3$ remains rhombohedral, the presence of the trigonal axis requires that all nitrates within a layer rotate in the same direction, but in the lower symmetry $CaCO_3$(II) phase, the loss of the trigonal axis removes this constraint. In $CaCO_3$(II), a given row of carbonate groups projected along the monoclinic *b* axis rotates in a clockwise direction, while adjacent rows in the same layer rotate in the opposite sense. These rotations are consistent with the direction

of the displacement of the calcium atoms parallel to one of the calcite ($10\bar{1}4$) planes. The orientation of this displacement is approximately 45° to that observed for the sodium atoms in the $NaNO_3$ transition.

In the calcite-type structure, the oxygen–oxygen distances are identical at all cation sites. In the $NaNO_3$ transition to the ferroelectric state, the coordinated motion of each sodium atom with its adjacent neighbors produces a situation in which the three sodium–oxygen bonds above the sodium are equal, but different from the three equal sodium–oxygen bond lengths below. It can be seen by examination of this motion [Fig. 5(*a*)] that the oxygen–oxygen separation has increased at all (*a*) and (*c*) sites, while decreasing at the (*b*) and (*d*) sites. This accommodates the cooperative displacive motion of the sodium atoms all in the same direction parallel to the threefold axis away from their $\bar{3}$ symmetry position.

In the calcite–$CaCO_3$(II) transition, however, the relative motion of the atoms is such that each of the six calcium–oxygen bonds have different lengths. For example, if calcium(*c*) moves toward oxygen(1) with component motion towards oxygen(3′) and away from oxygen(5), the strong interaction between calcium(*c*) and oxygen(3′) tends to be coupled with a clockwise rotation of the carbonate groups containing oxygen(1) and(3′). The interaction between calcium(*c*) and oxygen(5) results in a relaxation allowing the carbonate group containing oxygen(5) to rotate in the counterclockwise direction. The effect of calcium(*d*) can be analyzed in the same manner.

The average O–O separation in $CaCO_3$(II) has increased (3·419 Å) at the (*b*) and (*c*) sites and decreased (3·140 Å) at the (*a*) and (*d*) sites. The O–O distances at these sites range from a low of 3·043 to a high of 3·589 Å, with an overall average of $3{\cdot}280 \pm 0{\cdot}052$ Å, which agrees with the corresponding value for calcite of $3{\cdot}260 \pm 0{\cdot}006$ Å. These data are summarized in Table 6. Even though all calcium atoms are crystallographically equivalent, this model separates them into two distinct groups with respect to displacement direction as illustrated in Fig. 5(*c*) (bottom), where calcium(*a*) and (*b*) are displaced upward to the left, and calcium(*c*) and (*d*) are displaced downward to the right. Fig. 6 is an enlargement of the labeled section of Fig. 5(*c*) (top). From this illustration, it can be seen that the displacement of calcium(*a*) [calcium(*b*)] is antiparallel to calcium(*c*) [calcium(*d*)]. This is a consequence of the presence of one of the original *n*-glides [*c*-glide in $CaCO_3$(II)] retained from the calcite structure.

Table 6. *Interatomic distances* (Å) *in* $CaCO_3$(II) *compared with* $CaCO_3$(I) (*calcite*)

Atom designations refer to Fig. 6.

		$CaCO_3$(II), 15 kbar Average	Calcite,* 1 bar
C——O		1·256 ±0·050	1·283 ±0·002
O——O		2·170† ±0·038	2·222 ±0·004
Ca(*c*)–O(1)	2·319		
Ca(*c*)–O(5)	2·429	2·383 ±0·038	2·356 ±0·004
Ca(*c*)–O(3′)	2·329		
Ca(*d*)–O(1)	2·376		
Ca(*d*)–O(2′)	2·434	2·383 ±0·038	2·356 ±0·004
Ca(*d*)–O(6′)	2·339		
O(1)—O(6′)	3·043		
O(1)—O(2′)	3·067	3·140 ±0·054	3·260 ±0·006
O(2′)–O(6′)	3·311		
O(3′)–O(5)	3·167		
O(1)—O(5)	3·501	3·419 ±0·048	3·260 ±0·006
O(1)—O(3′)	3·589		

* Chessin, Hamilton & Post (1965).
† O–O distances in a CO_3 group.

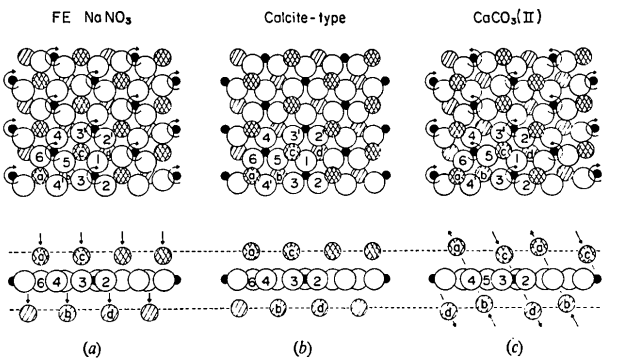

Fig. 5. (*a*) Rotational and translational displacements in the ferroelectric (FE) $NaNO_3$ phase transformation. (*b*) Anion layer of the calcite-type structure with cations above layer in (*a*) and (*c*) sites and those below layer in (*b*) and (*d*) sites. (*c*) Rotational and translational displacements in the $CaCO_3$(I)–$CaCO_3$(II) phase transformation. Note that the carbonates in adjacent rows rotate in opposite directions while calcium atoms are displaced parallel to the ($10\bar{1}4$) crystallographic plane as shown.

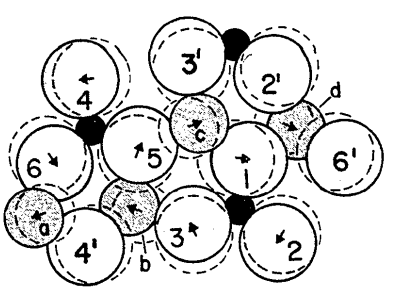

Fig. 6. An enlargement of the labeled region of Fig. 5(*c*) (top). The monoclinic *b* axis is parallel to a line connecting O(4) and O(4′).

Discussion

In this work, the space group $P2_1/c$ was selected for $CaCO_3$(II) on the basis of the observed symmetry. This assignment is also consistent with measurements of various physical properties. In an examination of the high-pressure phases of $CaCO_3$ by Raman spectra, Fong & Nicol (1971) detected a ν_2 (out-of-plane bend-

ing) mode in the $CaCO_3$(II) phase, suggesting a carbonate site symmetry c_1 in agreement with the $P2_1/c$ space-group assignment.

A noncentrosymmetric structure was proposed by Davis (1964), who suggested that $CaCO_3$(II) was isomorphous with ferroelectric KNO_3(III) as a result of his powder X-ray diffraction studies. The possibility of a ferroelectric state was checked by Samara (1974), who measured the dielectric constant of calcite up through the $CaCO_3$(I)–$CaCO_3$(II) phase boundary, and obtained a negative result which would be expected for a centrosymmetric space group.

The calcite $11\bar{2}3$ reflection, which both Jamieson (1957) and Davis (1964) reported missing from their $CaCO_3$(II) powder patterns, was present in both powder and single-crystal data in this study. In the previous powder studies, no new reflections were observed in this phase. Three new weak reflections were observed from powder studies in the present work. The reason why more new reflections are not observed in the powder pattern is because all the more intense new reflections in this region occur very near calcite reflections. Thus, little information on the structure of $CaCO_3$(II) is available from the powder data.

Since calcium carbonate and sodium nitrate both have the same structure at 1 bar, it is of interest to consider why they undergo such different displacive transitions. The high-pressure phase of sodium nitrate is ferroelectric, while $CaCO_3$(II) is anti-polar and may be considered antiferroelectric, depending upon the strength of its dipole–dipole interaction energy. The dynamics of the $CaCO_3$(I)–$CaCO_3$(II) transition are attributed to a soft phonon instability at the D point of the rhombohedral Brillouin zone boundary, as opposed to an instability at the zone center for the ferroelectric sodium nitrate transition. The difference in the nature of these transitions is related directly to the difference in lattice dynamics, which in turn are related to the relative strengths of the interatomic force constants. The details of this mechanism will be treated in a separate paper.

It is with pleasure that the authors thank Dr J. Dean Barnett of Brigham Young University for his reading of the manuscript and many helpful suggestions. Funds for the computer analysis of this work were made available by Dr Leo Vernon of Research Division at Brigham Young University. Thanks are also due to Dr Robert Collin of the University of Rochester for making available his precession camera, and for several useful discussions during the course of collecting the data.

References

BARNETT, J. D., PACK, J. & HALL, H. T. (1969). *Transactions of the American Crystallographic Association, Proceedings of the Symposium on Crystal Structure at High Pressure*, Vol. 5, pp. 113–131.

BELL, P. M. & ENGLAND, J. L. (1967). *Carnegie Inst. Wash. Year Book*, **66**, 354–356.

BOEKE, H. E. (1912). *Neues Jb. Miner. Geol.* **1**, 91–212.

BOETTCHER, A. L. & WYLLIE, P. J. (1968). *J. Geol.* **76**, 314–330.

BRIDGMAN, P. W. (1939). *Amer. J. Sci.* **237**, 7–18.

BUSING, W. R., MARTIN, K. O. & LEVY, H. A. (1971). *ORXFLS3. Crystallographic Structure-Factor Least-Squares Program*, Oak Ridge National Laboratory, Oak Ridge, Tennessee.

CHESSIN, H., HAMILTON, W. C. & POST, B. (1965). *Acta Cryst.* **18**, 689–693.

CLARK, S. P. (1957). *Amer. Min.* **42**, 564–566.

COHEN, L. H. & KLEMENT, W. (1973). *J. Geol.* **81**, 724–727.

CRAWFORD, W. A. & FYFE, W. S. (1964). *Science*, **144**, 1569–1570.

CRAWFORD, W. A. & HOERSCH, A. L. (1972). *Amer. Min.* **57**, 995–998.

CROMER, D. T. & MANN, J. B. (1968). *Acta Cryst.* A**24**, 321–324.

DAVIS, B. L. (1964). *Science*, **145**, 489–491.

EVANS, H. T. (1961). *Acta Cryst.* **4**, 689.

EVANS, R. C. (1952). *An Introduction to Crystal Chemistry*. Cambridge Univ. Press.

FONG, M. Y. & NICOL, M. (1971). *J. Chem. Phys.* **54**, 579–585.

GOLDSMITH, J. R. & NEWTON, R. C. (1969). *Amer. J. Sci.* **267**A, 160–190.

IRVING, A. J. & WYLLIE, P. J. (1973). *Earth Planetary Sci. Lett.* **20**, 220–225.

JAMIESON, J. C. (1953). *J. Chem. Phys.* **21**, 1385–1390.

JAMIESON, J. C. (1957). *J. Geol.* **65**, 334–343.

JOHANNES, W. & PUHAN, D. (1971). *Contrib. Miner. Petrol.* **31**, 28–38.

KONDO, S., SUITO, K. & MATSUSHIMA, S. (1972). *J. Phys. Earth*, **20**, 245–250.

MCDONALD, G. J. F. (1956). *Amer. Min.* **41**, 744–755.

MERRILL, L. & BASSETT, W. A. (1974). *Rev. Sci. Instrum.* **45**, 290–294.

MUELLER, M. H., HEATON, L. & MILLER, K. T. (1960). *Acta Cryst.* **13**, 828–829.

SAMARA, G. A. (1974). Personal communication.

SCLAR, C. B., CARRISON, L. C. & SCHWARTZ, C. M. (1962). *Amer. Soc. Mech. Eng. Paper* 62-*Wa*-248, 7 pp.

SIMMONS, G. & BELL, P. M. (1963). *Science*, **139**, 1197–1198.

VAN VALKENBURG, A. (1965). Conference Internationale sur-les-Hautes Pressions, Le Creusot, Saone-et-Loire, France, 2–6 August.

WEIR, C. E., BLOCK, S. & PIERMARINI, G. J. (1965). *J. Res. Natl. Bur. Stand.* **69**C, 275–281.

WANG, C. (1968). *J. Geophys. Res.* **73**, 3937–3944.

ZIMMERMAN, H. D. (1971). *Nature Phys. Sci.* **231**, 203–204.